Probing Pore Size Distribution by Cryogenic- and Relaxation 2H-NMR

5 AUTHORS, INCLUDING:

Eddy Walther. Hansen
University of Oslo
112 PUBLICATIONS 1,459 CITATIONS

SEE PROFILE

Reidar Haugsrud
University of Oslo
125 PUBLICATIONS 1,852 CITATIONS

SEE PROFILE

Henrik Ræder
SINTEF
30 PUBLICATIONS 288 CITATIONS

SEE PROFILE

ARTICLES

Probing Pore Size Distribution by Cryogenic- and Relaxation ^{2}H-NMR

E. W. Hansen,*,† C. Simon,‡ R. Haugsrud,‡ H. Raeder,‡ and R. Bredesen‡

Department of Chemistry, UiO, P.O. Box 1033 Blindern, 0315 Oslo, Norway, and
SINTEF Materials Technology, P.O. Box 124, Blindern, 0314 Oslo, Norway

Received: December 31, 2001; In Final Form: June 21, 2002

Cryogenic NMR and NMR spin−lattice relaxation time (NMRT) measurements of pore-confined water (D_2O) have been performed using *deuterium* NMR to probe the pore size distribution (PSD) of silica materials and porous membranes. NMRT measurements were performed at a temperature slightly below the normal freezing point (277 K) of bulk water (D_2O) to ensure that all interparticle water was frozen out. PSD derived from cryogenic NMR was in excellent agreement with PSD obtained from N_2-adsorption measurements. Also, PSD obtained by NMRT revealed approximately the same average pore dimension as obtained by N_2 adsorption. However, the former experimental technique resulted in somewhat narrower PSD than obtained by cryogenic NMR and N_2 adsorption and is discussed in the text. An attempt to determine the PSD of a TiO_2 membrane on a silica support by NMRT will also be discussed. The main results obtained in this work suggest that a combined use of cryogenic NMR and NMRT may give information on both PSD and pore-connectivity.

1. Introduction

Room temperature ^{1}H NMR relaxation time (NMRT) measurements of pore-confined fluids have been demonstrated as an important method for determining the pore-size distribution (PSD) of consolidated materials, like sandstone and concrete.[1−8] The technique is a valuable supplement to other principal techniques as mercury intrusion porosimetry (MIP), gas adsorption/desorption, small-angle scattering (light, X-ray, and neutron), and optical/electron microscopy. Of particular importance, NMR is nondestructive and does not require any kind of drying or vacuum treatment before testing. Actually, drying or evacuation may cause artificial changes to the structure of some materials.

An alternative technique to probe PSD of both consolidated and nonconsolidated materials is cryogenic NMR, as discussed by Hansen and co-workers.[9−12]

Concerning microporous materials, Fraissard et al.[13] explored several gases to probe PSD and discovered that the ^{129}Xe NMR chemical shift is exceptionally sensitive to pore size. Also, pulse field gradient (PFG) NMR[14,15] has been reported to probe pore characteristics of porous materials.

PSD derived from NMRT is based on a correlation between relaxation times (T_1 and T_2) of pore-confined fluid and the surface-to-volume ratio of the pore system.[5,16] For a certain pore geometry, like spherical and cylindrical pores, these relaxation rates are, to a first-order approximation, proportional to the inverse pore radius. A majority of reported measurements found in the literature have been performed on porous materials with simplified pore systems and narrow pore size distributions such as zeolites, different leached glasses, and packed spheres.[5,16−20]

Again, it is of importance to emphasize that when attempting to derive PSD from NMRT a second and independent experimental technique is required for calibration purposes; that is, a correlation between the actual NMR parameter to be monitored and pore size must be established. Bhattacharja et al.[19] used a surface relaxation parameter based on surfaces determined by nitrogen adsorption in their NMR pore size measurements. Gallegos et al.[8] concluded that an assumption or correction concerning pore geometry or surface layer volume was required.

Another difficulty relates to the existence of paramagnetic impurities, which may well affect the proton relaxation time of pore-confined fluids. For instance, it is known that the presence of paramagnetic ions such as iron or manganese on the grain surface is responsible for the enhancement of proton relaxation rates. In particular, Kleinberg et al.[21] emphasized that the proton relaxation rate of pore-confined fluids is not dominated by geometric restrictions (pore dimension) but by nucleus−electron interactions. Deuteron has a nuclear spin of 1 and, hence, possesses a nuclear quadrupole moment, implying that its relaxation behavior is affected by electric field gradients. Its magnetogyric ratio is about 6.5 times smaller than that of a proton. Theoretically, the paramagnetic contribution to $1/T_1$ is proportional to the square of the nuclear magnetogyric ratio, suggesting the relaxation time of deuteron to be much less affected by the existence of paramagnetic impurities than protons. Glasel at al.[22] have shown that the deuteron relaxation rate of D_2O mixed with glass beads (of dimension 20−660 μm) depends linearly on the inverse dimension of the glass beads. With this in mind, we decided to characterize some commercial silica samples (reference samples) by cryogenic NMR, NMRT, and N_2 adsorption. To the best of our knowledge, a critical comparison of PSD, as derived from these experimental techniques, have not been well documented. An important

* To whom correspondence should be addressed.
† Department of Chemistry, UiO.
‡ SINTEF Materials Technology.

Probing Pore Size Distribution

J. Phys. Chem. B, Vol. 106, No. 48, 2002 **12397**

advantage with the NMR techniques is that "nonconsolidated" materials or powder materials can be readily investigated.

One object of the present work is to compare cryogenic NMR and NMRT (*using deuterium as a probe nucleus*) with N_2 adsorption/desorption to probe PSD. A practical advantage of the latter techniques (NMRT) is its experimental simplicity and its short, overall acquisition time, of the order of minutes.

The NMR methods discussed will be extended to PSD analysis of a TiO_2 membrane on a silica support.

2. Experimental Section

2.1. Materials. The porous materials selected in this work were three commercial powder samples of silica denoted S40, S60, and S100 (Merck) with nominal pore diameters of approximately 40, 60, and 100 Å, respectively. All materials were heated under a vacuum for 1 h at 433 K before testing. The deuterated water was of 99.9% purity (Aldrich).

Additionally, a ultrafiltration titania supported disk membranes with a diameter of 38 mm were kindly offered by Kera-Nor (Norway). Nonsupported titania membranes were prepared from hydrolysis of titanium tetraethoxide as explained in ref 23. The sol was dried in a petri dish at room temperature for 24 h and sintered in air at 450 °C for 1 h. The amount of paramagnetic species within the silica samples was evaluated using ICP-AES. Only Fe was detected and corresponded to approximately 60 mg/kg for each sample. This amount of Fe impurity will have no significant effect on the deuterium relaxation rate of the solvent (D_2O) and will be discussed later (section 3.4).

2.2. Nitrogen Isotherms. The adsorption/desorption isotherms of nitrogen were acquired with a Carlo Erba Milestone 100 instrument. A thermistor probe controlled the temperature of the liquid-nitrogen bath. Each sample was degassed at 433 K for 1 h until a pressure of approximately 7 Torr was attained. The desorption step was initiated after a saturation pressure of 760 Torr was reached.

2.3. NMR. *2.3.1. Spin−Lattice Relaxation Time.* ^2H NMR spin−lattice relaxation rates were measured on a Varian VXR spectrometer operating at 46.044 MHz resonance frequency (corresponding to a proton resonance frequency of 300 MHz) at a temperature slightly below the normal freezing point of bulk water. All samples contained a surplus of deuterated water to ensure complete filling of the pores. This approach results in formation of a "slurry" of silica particles in water.

Each sample was initially cooled to 258 K within the magnet to ensure complete freezing of interparticle water. The temperature was then raised to a temperature just below the normal freezing point of bulk water (277 K for D_2O) to ensure that no signal arises from bulk water confined within the interparticle space. The stability of the temperature was estimated to be better than ±0.5 K. A bandwidth of 100 kHz, an acquisition time of 50 ms, and a 90° radio frequency (rf) pulse of 14.5 μs were applied with a repetition time of 1 s between successive scans. The number of transients applied in each experiment was varied between 4 and 64 scans as dictated by the required signal-to-noise ratio. The free induction decay (FID) was acquired after blanking the receiver for 20 μs in order to ignore the signal from the solid ice phase. Solid ice is known to have a very short spin−spin relaxation time of the order of a few microseconds. All measurements were performed using a conventional inversion recovery (180° − τ − 90°) pulse sequence. The delay time τ between the initial 180° pulse and the subsequent 90° read pulse was varied between 0 and 2 s in a random order. A total of 70 τ values were used. The reason for selecting τ values in a random order was found necessary in order to avoid any systematic errors when deriving spin−lattice relaxation times.

2.3.2. Cryogenic NMR. The temperature was changed in steps of 1 K. A temperature equilibration of 2 min was applied before any spectrum was acquired. This seemingly short equilibration time resulted in a signal intensity that did not differ significantly from the corresponding signal intensity observed after 5−10 min of temperature equilibration.[10] One exception to this observation concerns bulk, solid ice (D_2O), which, just above its normal melting point of 277 K, requires more than 20 min to melt. This is, however, of no concern in this work.

The signal intensity of the resonance peak was determined by numerical integration and corrected for temperature (*T*) according to the Curie's law.[24] This simply involves a scaling of the observed NMR signal intensity, measured at a temperature *T*, by a factor T/T_0 (with $T_0 = 277$ K). The ^2H NMR signal intensity as a function of the inverse absolute temperature (IT curve) was monitored by sampling NMR spectra during heating from some initially "low" temperature and up to 282 K in steps of 1 K. The reason for using the heating curve rather than the cooling curve originates from the significant supercooling of pore-confined water during cooling, which displays the two curves relative to each other. Moreover, the heating curve was more reproducible than the corresponding cooling curve.

In these experiments, both temperature calibration and temperature control are of importance. Hence, these aspects of the experimental procedure are considered with particular care as detailed in a previous paper;[10] That is, methanol inside a capillary tube (the NMR thermometer) is placed within the porous sample, which in turn is placed inside the NMR magnet. The temperature is recorded as a function of setting temperature and time of temperature equilibration. When changing the temperature in steps of 1 K, an equilibration time of 2 min was found to be sufficient to reach, within experimental error, a constant and time independent temperature within the sample.

3. Results and Discussion

3.1. Nitrogen Isotherms. The adsorption/desorption isotherms of nitrogen at 77 K are shown in Figure 1 for all three samples. The shape of the isotherms are typical for capillary condensation in mesopores (type IV), as indicated by the steep slope at relative pressures $p/p_0 > 0.35$. The hysteresis loop can be classified as type A, which are attributed to *cylindrical* pore geometry. Selecting porous materials having well-defined and simple pore geometry is of main importance when comparing PSD obtained from different experimental techniques.

The small volume increment observed at high relative pressure ($p/p_0 > 0.95$, Figure 1) is attributed to inter particle volume. The true volume of pore-confined nitrogen was determined by subtraction and are tabulated in Table 1. All gas-volumes are referred to standard pressure and temperature (STP).

To determine the specific surface area (*S*) and the average pore size (R_{av}) of the samples, the Brunauer−Emmett−Teller[25] (BET) equation (eq 1) was applied:

$$\frac{1}{V[(p_0/p) - 1]} = \frac{1}{V_m C} + \frac{C - 1}{V_m C}(p/p_0) \tag{1}$$

V is the volume of nitrogen adsorbed at a relative pressure p/p_0 and V_m is the volume of adsorbate constituting a monolayer of surface coverage. The term *C* (the BET constant) is related to the energy of adsorption in the first adsorbed layer and consequently its value is an indication of the adsorbent/adsorbate interaction. Because the chemical/physical surfaces of the three reference materials are tentatively identical, it is reason to believe that *C* is the same for all materials.
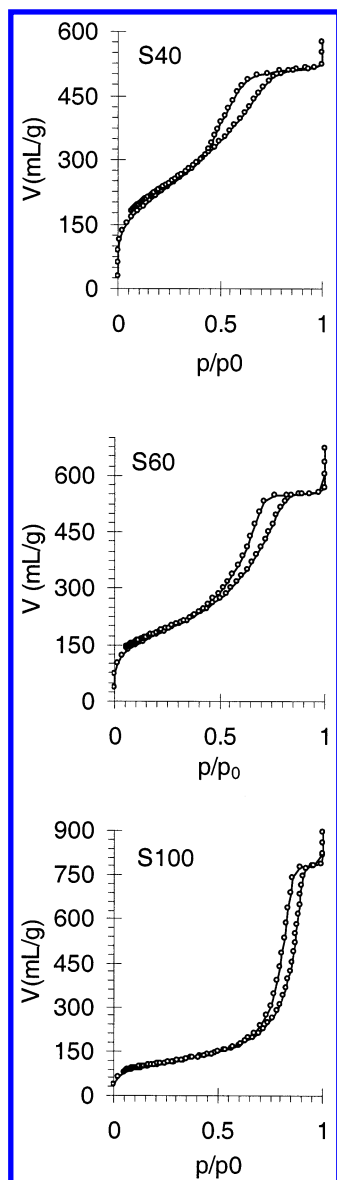
Figure 1. Adsorption/desorption isotherms (nitrogen) of porous silica glasses; S40, S60, and S100, respectively. *V* represents the volume of nitrogen at standard temperature and pressure (STP), and p/p_0 represents the relative pressure.

TABLE 1: Total Adsorbed Volume (V_{tot}) of Nitrogen, Volume of Nitrogen Monolayer (V_m; eq 1), and Specific Surface Area S_m [a] of Samples S40, 60, and S100[b]

sample	$V_{tot}(cm^3/g)$	$V_m(cm^3/g)$	$S_m(m^2/g)$
S40	515	180.0	645
S60	550	141.7	517
S100	780	83.3	303

[a] $S_m = n_{monolayer}NA_{cs}(1 - p/p_0)/RT$ where $n_{monolayer}$ is the number of moles of nitrogen adsorbed on the surface within one monolayer at a pressure p_0. N, A_{cs}, R, and T are the Avogadro number ($=6.023 \times 10^{23}$ molecules mol^{-1}), the cross-sectional area for nitrogen ($=1.62 \times 10^{-19}$ m^2 molecule^{-1}), the gas constant ($=8.2054 \times 10^{-5}$ m^3 atm mol^{-1} K^{-1}), and the absolute temperature ($=300$ K), respectively. [b] All volumes are referred to STP (standard temperature and pressure).

The solid curves in Figure 2A were obtained by a simultaneous, linear least-squares fit to eq 1 (with $y = 1/[V(p/p_0 - 1)]$ and $x = p/p_0$) within the relative pressure range $0.1 < p/p_0 < 0.45$, assuming the BET constant C to be the same for all three materials. The C value was found to be 187.5 and resulted in an excellent fit to the observed data (Figure 2A).
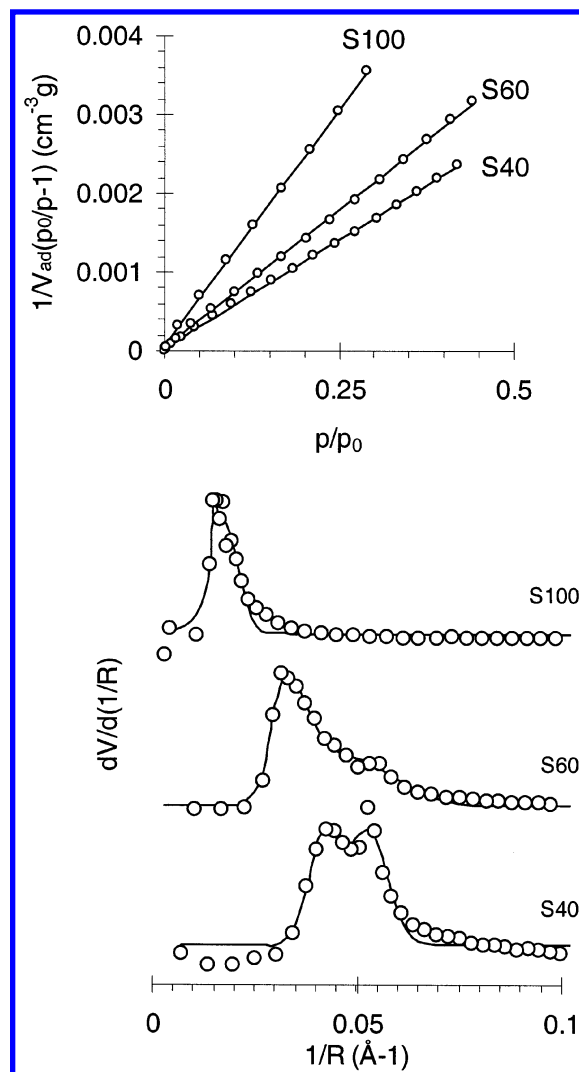

Figure 2. (A; top) $Y = 1/V [(p/p_0) - 1]$ as a function of $x = p/p_0$. V represents the volume of nitrogen adsorbed at a relative pressure of p/p_0. The straight lines represent linear least-squares fits to eq 1. (B; bottom) PSD (o) of samples S40, S60, and S100 as derived from N$_2$-desorption data in Figure 1. Solid curves represent Gaussian, nonlinear model fits to the observed data.

The monolayer volume V_m and the specific surface area S derived from the BET analysis are tabulated in Table 1. Also, the total volume V_{tot} of nitrogen absorbed is depicted in Table 1. Because the pore geometry is cylindrical (implicit assumption when using the BET approach), the average inverse pore radius ($1/R_p$) was determined from eq 2:

$$\frac{1}{R_p} = \frac{S}{2V^{liq}} \tag{2}$$

where V^{liq} represents the maximum volume of liquid nitrogen within the pores. This parameter is simply calculated from the equation $V_{liq} = PV_{tot}V_M/RT$ where V_M represents the molar volume of the liquid adsorbate (34.7 cm^3/mol for nitrogen) and P is the ambient pressure. The results are summarized in Table 1.

Using the method proposed by Barrett, Joyner, and Halenda (BJH),[26] the inverse pore radius ($1/R$) can be determined from the relative pressure p/p$_0$ according to eqs 3a–3c:

$$\frac{1}{R} = \frac{1}{r_K + t} \tag{3a}$$

Probing Pore Size Distribution

J. Phys. Chem. B, Vol. 106, No. 48, 2002 **12399**

where r_K (eq 3b) is the Kelvin radius and t (eq 3c) defines the thickness of one layer of nitrogen molecules

$$r_K = -\frac{2\gamma V_M}{RT \ln(p/p_0)} \tag{3b}$$

$$t = a\left[\frac{1}{\ln(p_0/p)}\right]^{1/b} \tag{3c}$$

γ is the surface tension of nitrogen at its boiling point (8.85 ergs cm^{-2} at 77 K), V_M is the molar volume of liquid nitrogen (34.7 cm^2 mol^{-1}), $a = 6.0533$, and $b = 3.0$. From these equations, the PSD can be calculated.

We would like to emphasize that there are ongoing discussions within the scientific community regarding the validity of the BJH model to determine PSD. The general approach when aiming at estimating PSD from nitrogen adsorption studies is based on the Kelvin equation (eq 3b) corrected by adding a statistical thickness function (t function) of the adsorbate film (eq 3c). It has been argued that the BJH method underestimates the pore diameter, when applying a t function of the form represented by eq 3c. Hence, during the past decade, alternative representations of the t function within the BJH model have been proposed.[27,28] To our knowledge, the question related to the type of t function to be implemented in the BJH model is still controversial.

We will in a later section (section 3.3) see that an alternative choice of a t function will have no significant effect on the results presented in this work.

The derived PSDs are plotted in Figure 2B. The solid curves represent nonlinear least-squares fits to a sum of two Gaussian functions, $g(1/R)$:

$$g(1/R) = \sum_{i=1}^{2} \frac{I}{\sqrt{2\pi}\sigma_i} \exp\left[-\left(\frac{1/R - \overline{1/R_i}}{\sqrt{2}\sigma_i}\right)\right] \tag{4a}$$

in which $\overline{1/R_i}$, σ_i, and I_i represent the average inverse pore radius and the width and the intensity of the Gaussian function i (see eq 4a). As can be inferred from Figure 2B, this model fit gives a reasonable representation of the observed PSD. Because of the limited number of data points, there was no statistical arguments to fit the data to more than two Gaussian functions. Also, other types of distribution functions may be used, as for instance a log−normal distribution function. However, because the shape function is, a priori, unknown, a Gaussian distribution function was chosen mainly because of its mathematical simplicity. The average inverse pore radius ($1/R_G$) was estimated according to eq 4b:

$$1/R_G = \frac{\sum_i \int_0^\infty 1/R \cdot g_i(1/R)\, d(1/R)}{\sum_i \int_0^\infty g_i(1/R)\, d(1/R)} = \frac{\sum_i \overline{1/R_i} \cdot I_i}{\sum_i I_i} \tag{4b}$$

The average values $1/R_G$ of samples S40, S60, and S100 are shown in Table 2.

Rather encouraging, the derived inverse pore radii $1/R_P$ and $1/R_G$ are, within experimental error (estimated to be within ±10%), the same. The reason for using the inverse pore radius rather than the pore radius itself will become evident in the next sections.

TABLE 2: Average Inverse Pore Radius ($1/R_p$) Obtained by a Simple BET Analysis (eq 2) and Corresponding Inverse Pore Radii $1/R_i$ ($i = 1$ and 2) and $1/R_G$, as Derived from Nonlinear Least Squares Fits of eqs 5a and 5b to the Observed PSD in Figure 3, Respectively

sample	$1/R$ (Å^{-1})	$1/R_p$ (Å^{-1})[a]	$1/R_G$ (Å^{-1})
S40	0.055	0.047	0.048
	0.042		
S60	0.044	0.035	0.036
	0.031		
S100	0.017	0.015	0.017
	0.015		

[a] The uncertainty is estimated to be better than approximately 3%.

TABLE 3: Transition Temperature ($X = 1000/T$) and Spin−Lattice Relaxation Rate ($1/T_1$) of Pore-Confined D$_2$O within Samples S40, S60, and S100

sample	$X = 1000/T$ (K^{-1})	intensity (%)	$1/T_1$[a] (s^{-1})	intensity (%)	$1/T_1$[b] (s^{-1})
S40	3.947	63	22.6	17	13.0
	3.835	37	12.0	83	
S60	3.887	43	15.9	20	11.5
	3.776	57	10.5	80	
S100	3.719	49	7.19	23	5.9
	3.675	51	5.49	77	

[a] Discrete model (eq 8). [b] Continuous model (eqs 9−11).

3.2. Cryogenic NMR. How the melting-point distribution curve, dI/dX (with $X = 1000/T$) of solid ice (H$_2$O) confined in porous materials can be derived from the observed IT curve, $I(X)$, is thoroughly discussed in previous studies.[9−11] The theoretical model used to derive this distribution curve is of general validity and not only limited to solid water (H$_2$O). The theory has been extensively discussed elsewhere,[9−11] so only the main (two) equations of importance to this work (eqs 5a and 5b) will be reported without further comments:

$$I(X) = \sum_{i=1}^{N} \frac{I_{01}}{\sqrt{\pi}} \int_{-\infty}^{(X - X_{ci})/\sqrt{2}\Delta_i} \exp[-u^2]\, du \tag{5a}$$

$$\frac{dI}{dX} = \sum_{i=1}^{N} \frac{I_{01}}{\sqrt{2\pi}\Delta_i} \exp\left[-\left[\frac{X - X_{ci}}{\sqrt{2}\Delta_i}\right]^2\right] \tag{5b}$$

Figure 3A shows the IT curve of sample S100 during a heating−cooling cycle and reveals a significant hysteresis effect. This is typical for a macroscopic freezing phenomenon in which part of the fluid becomes solid. Because the melting point transition is better reproduced than the freezing point transition, only the melting point distribution curve is acquired and analyzed.

The IT curves of all three samples S40, S60, and S100 are plotted in Figure 3B together with the IT curve of sample X, which represents a pure, porous TiO$_2$ membrane material. The solid curves represent model fits to eq 5a ($N = 2$). No statistical improvement (significance tests) was obtained when fitting the present model with $N > 2$. The derived transition temperatures are tabulated in Table 3.

The calculated melting point distribution curves (eq 5b) of solid D$_2$O within samples S40, S60, S100, and X are displayed in Figure 3C. A significant relative displacement toward lower temperatures with decreasing average pore size is seen. The melting point distribution of the membrane material is positioned between the distribution curves of samples S60 and S100,
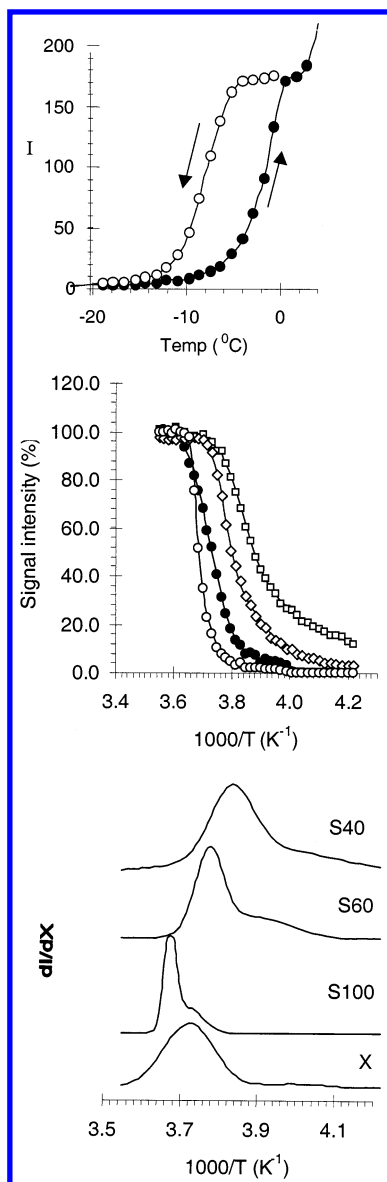
Figure 3. (A; top) IT curve of D_2O confined in sample S40 during a cooling ($\bigcirc$)/warming ($\bullet$) cycle. An hysteries effect is clearly visualized. The solid curves represent model fits to eq 5a. (B; middle) IT curves (warming) of D_2O confined in samples S40, S60, X, and S100 (from right to left). Solid curves represent model fits to eq 5a. (C; bottom) Melting point distribution curves of samples S40, S60, S100, and X as derived from the observed IT curves in Figure 5 by use of eq 5b.

suggesting a pore dimension somewhere between the pore dimension of the two reference samples. This topic will be addressed in the next section.

3.3. Correlation between Pore Size and Melting Point Transition. The well-known Gibbs−Thompson[29,30] equation, which relates pore dimension (R) to melting point suppression (Δt) of pore-confined solids can be written

$$\Delta t = T_0 - T = K\frac{1}{R - d} \tag{6a}$$

K is considered a constant, and d represents the thickness of an interface layer, located between the solid matrix and the solid ice within the pore. T_0 is the melting temperature of bulk, solid D_2O (=277 K), and T is the melting temperature of pore-confined D_2O. Additional details and discussion concerning this equation can be found in the list of references.[9−12]
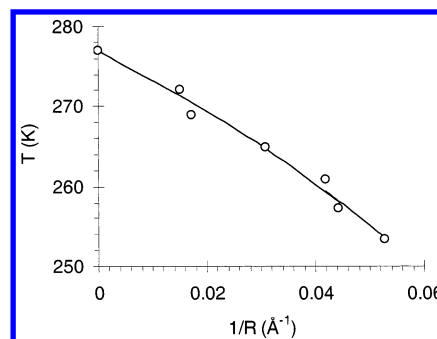

Figure 4. Melting temperature (T) of D_2O confined in samples S40, S60, and S100 (as obtained by cryogenic NMR) as a function of the inverse pore radius $1/R$ (as obtained by N_2 adsorption). The solid curve represents a model fit to eq 6b.

Recalling that each of the materials S40, S60, and S100 possess a bimodal PSD (Table 2) and reveal two distinct transition temperatures of pore-confined solid D_2O during warming (Table 3), the latter parameter (T) is plotted against $1/R$ in Figure 4. By rearranging eq 6a, we obtain eq 6b:

$$T = T_0 - K\frac{1}{R}\frac{1}{1 - d/R} \tag{6b}$$

This equation predicts a linear decrease in melting temperature of pore-confined fluid with increasing inverse pore radius ($1/R$) for $d/R \ll 1$. When the ratio d/R becomes larger (but <1), the predicted transition temperature will decrease more strongly than predicted by the simple linear behavior. This is exactly what is observed in Figure 4. The solid curve represents a model fit to eq 6b, with $K = (354 \pm 43)$ K Å^{-1} and $d = (3.8 \pm 2.2)$ Å. These numbers agree rather well with the values of $K = (355 \pm 17)$ K Å^{-1} and $d = (5.9 \pm 0.3)$ Å obtained on identical materials saturated with normal water (H_2O).[12]

If replacing the t function, represented by eq 3c, by an alternative function as published by Kruk and co-workers,[28] the derived K value remains unchanged while the d value increases to $d = (5.3 \pm 2.7)$ Å. A significance test shows, however, that the two t functions (differing by a constant term k of 3 Å) do not result in statistically different d values. Hence, the original t function in the BJH model (eq 3c) is applied throughout in this work.

At a temperature of 1 °C below the normal melting point of bulk ice (D_2O), eq 6 predicts that water confined in pores larger than approximately 350 Å will exist as solid ice. The value 350 Å gives a "practical" upper limit of pore dimensions (radius) which can be probed by cryogenic NMR using D_2O as a probe molecule.

Equation 6b makes it possible to derive the PSD (dI/dR) from the melting point distribution curve dI/dX, by noting that

$$\frac{dI}{dR} = \frac{dI}{dX}\frac{dX}{dR} \tag{7a}$$

The term dX/dR can be found from eq 6a ($X = 1000/T$) and results in the following mathematical expression for the PSD:

$$\frac{dI}{dR} = \frac{1000}{K}\left[\frac{X}{X_0} - 1\right]^2\frac{dI}{dX} \tag{7b}$$

The derived PSD is plotted in Figure 8. The dotted curves represent PSD determined by N_2 adsorption. Considering the inherent assumptions and simplifications made in deriving eq 7b (K and d are constants and independent of temperature), the
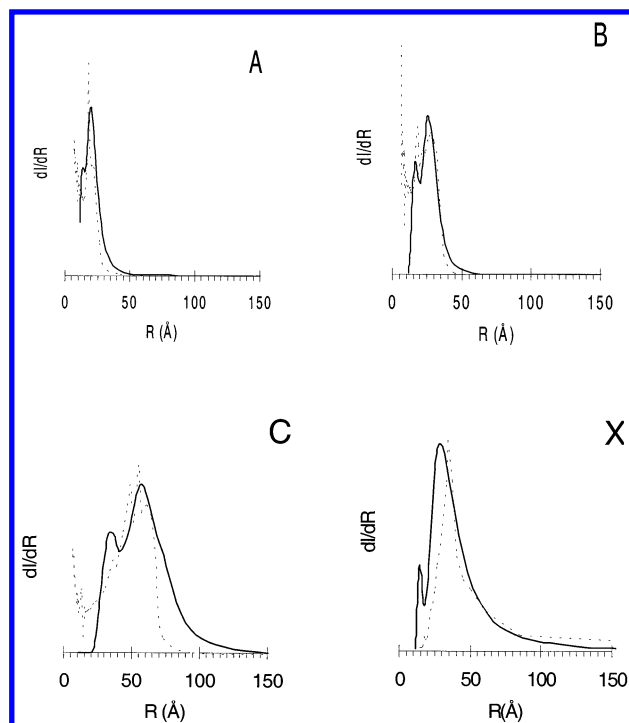
Probing Pore Size Distribution

J. Phys. Chem. B, Vol. 106, No. 48, 2002 **12401**

Figure 5. PSD of samples S40 (A), S60 (B), S100 (C) and a pure TiO_2 membrane (X) as obtained by N_2 adsorption (- - -) and cryogenic NMR (——). See text for further details.

predicted PSD derived from cryogenic ^2H NMR is in surprisingly good agreement with the corresponding PSD determined by N_2 adsorption.

Also, the PSD of a porous membrane material (sample X), as derived from eq 7b, reveals an average pore dimension of 35 Å (Figure 5; solid curve). Within experimental error, this average pore size is the same as obtained by N_2 adsorption (dotted curve in Figure 5X). How to obtain PSD from relaxation time measurements will be the subject in the next sections.

3.4. Spin-Lattice Relaxation Time Analysis. When acquiring a ^2H NMR spectrum of a slurry composed of water (D_2O) and silica particles (saturated with D_2O), the signal intensity from the interparticle water may dominate the spectrum. This will make NMR analysis of pore-confined water difficult and highly unreliable. To overcome this problem, cooling the sample just below the normal freezing point of bulk water (277 K; D_2O) will freeze out the interparticle water (as solid ice). Because of the very short spin−spin relaxation time of solid ice (few microseconds), this phase will be unobservable by the present NMR technique. It is thus important to acquire ^2H NMR spectra at a temperature as close to the freezing point of bulk water as possible, to maximize the observable range of pore sizes. Each sample investigated in this work is subjected to the same thermal procedure, i.e., cooling to 258 K and then heating to a temperature just below the melting point (276 K) of bulk ice (D_2O).

Using ICP-AES, the amount of paramagnetic species was determined to be less than 5 mg/kg, except for Fe, which revealed a value of approximately 60 mg/kg for all samples. Because the pore volume of the different porous silica samples is approximately 1 cm^3/g, it follows that the concentration C_{Fe} of Fe in the pore water will be approximately 0.3 mM. This concentration was estimated by assuming all Fe within the silica to be dissolved in the pore fluid. This concentration will represent the maximum concentration of Fe in the pore-confined water. From the work of Kowalevski et al.,[34] the relaxivity of

Fe^{3+} at 300 MHz is approximately 4.5 mM^{-1} s^{-1} and corresponds to a contribution to the spin−lattice relaxation rate of approximately 1.4 s^{-1}. For deuterium, which has a gyromagnetic ratio of only 3/20 of the proton nucleus, the spin−lattice relaxation rate contribution will be less than 0.3 s^{-1}. Actually, if the concentration of iron were 3−4 times larger, i.e., 200 mg/g, its effect on the deuterium spin−lattice relaxation rate would be insignificant. A concentration of such a magnitude would not affect the relaxation rate of the solvent D_2O to any significant degree.

However, if the Fe impurity was located on the surface of the particles or confined within the silica framework, and thus immobilized, the effect on the deuterium spin−lattice relaxation rate of the solvent water molecules would be even smaller (assuming fast exchange conditions). This conclusion implicitly assumes that Fe is homogeneously distributed throughout the silica particles. In the case that the Fe impurity is not homogeneously distributed, it is difficult, if not impossible, to say anything definite about the relaxation rate of the solvent D_2O. There is, however, no reason to believe that Fe is not homogeneously distributed within the silica. Hence, the existence of paramagnetic impurities and its effect on the relaxation rate of the solvent water (D_2O) is believed to be of only marginal importance in this work.

In the next section, two different relaxation time models will be presented.

3.4.1. Discrete Relaxation Model. Figure 6A shows the NMR spin−lattice relaxation curves (longitudinal magnetization vs interpulse timing; τ) of the three porous reference samples investigated. For a discrete relaxation model with N number of spin−lattice relaxation rates, $1/T_{1i}$ ($i = 1 - N$), the relaxation curve $M(\tau)$ can be expressed as a sum of exponential functions (eq 8):

$$M(\tau) = \sum_{i=1}^{M} M_{0i}[1 + \alpha \exp(-\tau/T_{1i})] \quad (8)$$

corresponding to N "regions" of water molecules with characteristic relaxation rates $1/T_{1i}$. M_{0i} represents the equilibrium magnetization of component i, and α is an adjustable parameter which takes account for inhomogeneities in the rf pulse. In general, α is expressed by $\alpha = (2\sum \cos \theta_j)/m$, where m is the number of spins disturbed by the rf pulse and Θ_j is the pulse angle of the j spin. For perfect pulses, Θ_j is 180° for all spins, implying that $\alpha = -2$.

A critical, statistical evaluation of the relaxation curves shows that they are all best fitted to a double exponential function ($N = 2$), as illustrated by the solid curves in Figure 6A. The difference between observed and calculated signal intensity (residual) is plotted as a function of time in Figure 6B. These residuals seem to be randomly distributed. The relaxation rates ($1/T_1$) are tabulated in Table 3.

3.4.2. Continuous Relaxation Model. If introducing a distribution $f(1/T_1)$ of relaxation rates ($1/T_1$), the relaxation curve $M(\tau)$ (eq 8) can be generalized to give the following expression:

$$M(\tau) = \int_{1/T_{1B}}^{1/T_{1s}} M_0 [1 - \alpha \exp(-\tau/T_1)] f(1/T_1) \, d(1/T_1) \quad (9)$$

Equation 9 is a Fredholm integral equation of the first kind, and the recovery of the distribution function is known to be an ill-posed problem.[32,33] With this in mind, we introduced a simple analytical approach to circumvent this problem. Because the shape function is a priori not known, we decided to select an adequate and simple function, enabling an analytical expression
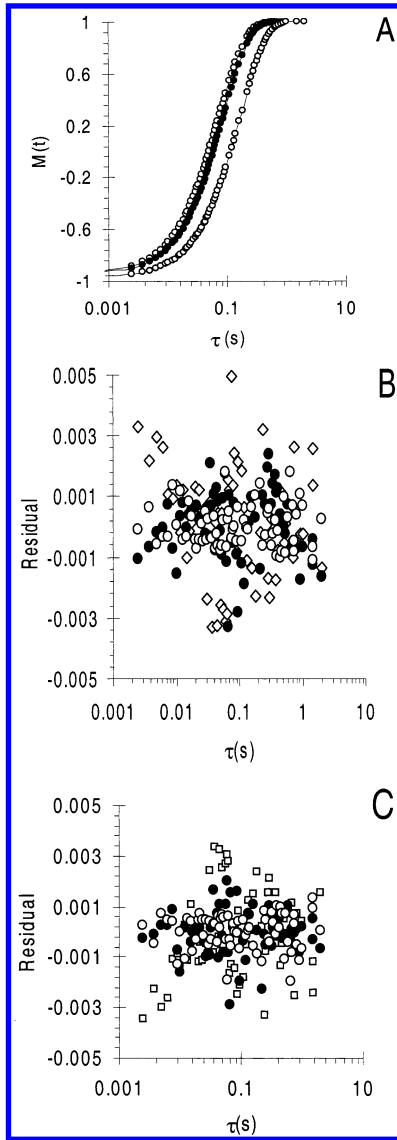
Figure 6. (A) Spin−lattice relaxation curves of D_2O confined in samples S40, S60, and S100 (from left to right). Solid curves represent model fits to eqs 8 (discrete relaxation model, with $N = 2$) and 11 (continuous relaxation model), respectively. The residual fits are displayed in B (discrete relaxation model) and C (continuous relaxation model), respectively.

of $M(\tau)$ to be derived. A relevant choice of a shape function is a sum of Gaussian functions, analogous to eq 4a, i.e.

$$f\left(\frac{1}{T_1}\right) = \sum_i \frac{I_i}{\sqrt{2\pi}\sigma_i} \exp\left[-\left(\frac{1/T_1 - 1/T_{1i}}{\sqrt{2}\sigma_i}\right)2\right] \quad (10)$$

where $\overline{1/T_{1i}}$ is the average relaxation rate and σ_i and I_i represent the width and intensity of the Gaussian function i. Inserting eq 10 into eq 9 gives, after some simple but tedious algebra (Appendix), the following expression:

$$M(\tau) = M_0 \sum_{i=1}^N \left[\begin{array}{l} \int_{x_B}^{x_s} \frac{1}{\sqrt{2\pi}\sigma_i} \exp\left[-\left(\frac{x - \overline{x_i}}{\sqrt{2}\sigma_i}\right)^2\right] dx - \\ \alpha e^{\beta_i} \int_{x_B}^{x_s} \frac{1}{\sqrt{2\pi}\sigma_i} \exp\left[-\left(\frac{x - \overline{x'_i}}{\sqrt{2}\sigma_i}\right)^2\right] dx \end{array} \right] \quad (11)$$
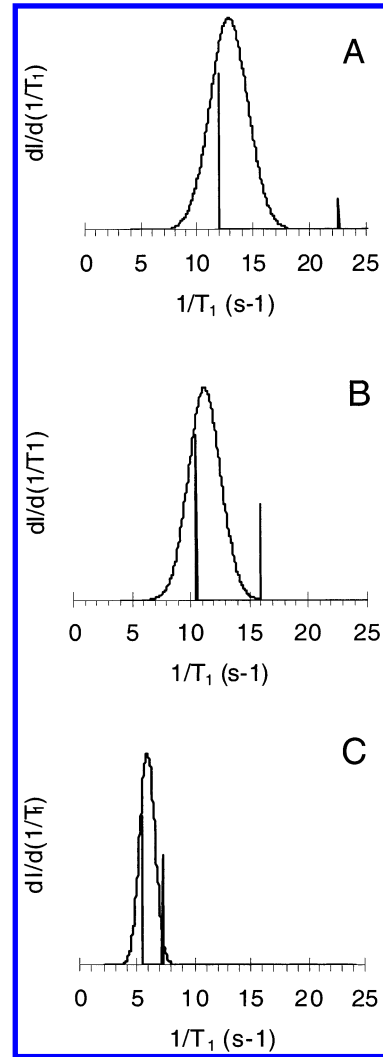

Figure 7. Spin-lattice relaxation rate distributions of D_2O confined in samples S100, S60, and S40 (from top to bottom) as obtained by the continuous relaxation model (continuous curves) and the discrete relaxation model (stick spectrum) via eqs 10 and 8.

where $x_s = 1/T_{1s}$, $x_B = 1/T_{1B}$, $x = 1/T_1$, $\overline{x_i} = \overline{1/T_i}$, $\overline{x'_i} = \overline{x_i} - \sigma_i^2\tau$ and $\beta_i = \sigma_i^2\tau^2/2 - \tau\overline{x_i}$. Equation 11 was fitted to the relaxation curves of sample S40, S60, and S100. The residuals are plotted in Figure 6C and shows a random error distribution of the same magnitude as observed for the discrete relaxation model (Figure 6B). The actual relaxation time distributions are shown in Figure 7 together with the relaxation rates derived from the discrete relaxation model (vertical lines). How to derive PSD from a continuous relaxation model will be discussed in the next sections.

3.5. Relation between Pore Radius (R) and Spin−Lattice Relaxation Time (T_1). To derive a PSD from spin−lattice relaxation time measurements, a relation between pore radius and spin−lattice relaxation time is needed.

The simplest physical model describing a two-phase molecular system is a "two-fraction, fast-exchange" model proposed by Zimmerman and Brittin.[34] This model assumes two magnetically distinct systems or phases; a bulk phase with a relaxation time $T_{1,b}$, and a phase close to the pore surface with a much shorter relaxation time, $T_{1,S}$, i.e.

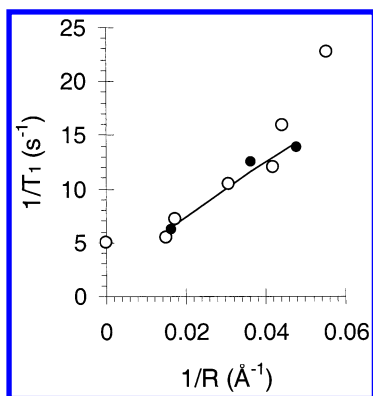$$\frac{1}{T_1} = \frac{f}{T_{1b}} + \frac{1-f}{T_{1,S}} \quad (12a)$$

Figure 8. Spin-lattice relaxation rate ($1/T_1$; NMRT) as a function of the inverse pore radius ($1/R$; N_2 adsorption) as obtained by the discrete relaxation model (○) and the continuous relaxation model (●). The solid curve represent a best model to the relaxation rates obtained by the continuous relaxation model via eq 12d with $d = 3.8$ Å (as taken from cryogenic NMR). See text for further details.

where f represents the mole fraction of "bulk" fluid

$$f = 1 - S\,d/V \tag{12b}$$

where d is the thickness of the surface layer characerized by the relaxation rate $1/T_{1s}$. S and V represent the surface area and the pore volume, respectively. For certain well-defined pore geometries, the parameter f can be expressed by the pore radius R according to

$$f = (1 - d/R)^n \tag{12c}$$

where $n = 2$ for cylindrical pores and $n = 3$ for spherical pores. Hence, eq 12a can be written

$$\frac{1}{T_1} = \frac{1}{T_{1S}} + \left[\frac{1}{T_{1B}} - \frac{1}{T_{1S}}\right][1 - d/R]^n \tag{12d}$$

Figure 8 shows a plot of the spin−lattice relaxation rate (Table 3) as a function of the inverse pore radius (Table 2). The open circles represent relaxation rates derived from the discrete relaxation model and the black dots represent average relaxation rates as obtained from the continuous relaxation model. The larger spread in data points obtained from the former (discrete relaxation model) model is believed to arise from pore connectivity, i.e., fluid molecules diffusing between pores. One observation supporting the existence of molecular diffusion between pores (pore connectivity) is that the ratio of the signal intensity of the two components observed from cryogenic NMR and NMRT, respectively, are significantly different (Table 3).

In general, there are four factors affecting the spin−lattice relaxation rate of pore-confined fluid, i.e., (1) exchange of pore-confined fluid molecules between the surface and the rest of the pore, (2) surface relaxivity ($d\,1/T_{1s}$), (3) pore geometry, and (4) pore-connectivity, i.e., how fast fluid molecules diffuse between pores on a NMR time scale.

The exchange of pore-confined molecules is expected to be in the fast exchange limit (on the NMR time scale) and simply results in a single relaxation rate as described by eq 12a.

The second factor is determined by the interaction strength of fluid molecules and the surface molecules of the matrix. Not surprisingly, if two materials are of the same chemical composition, both d and T_{1s} are expected to be the same for the same pore-confined fluid.

Strictly speaking, the spin−lattice relaxation rate is actually dependent on the surface-to-volume ratio (S/V; eqs 12a and

12b). Hence, to determine pore size, the actual pore geometry has to be known. If the pore shape is irregular, i.e., not pure cylindrical or spherical, it is still possible to approximate the pore size by such a simple geometric shape. As a consequence, when using eq 12d to estimate pore dimension of pores having irregular geometric shape, the pore size may be more or less biased. However, as will become clear later, such a systematic error may be compensated by calibration.

Of particular concern, however, is the effect of pore connectivity. In this respect, the diffusivity of the fluid molecules is of crucial importance. First, assume that two neighboring cylindrical pores of different radii R_1 and R_2 to be coupled and that fluid molecules diffuse between these pores with a rate slow on the NMR time scale. Then, the two pore sizes can be extracted separately because the relaxation curve (eq 12d) can be deconvoluted into two relaxation times. If, however, the diffusion is fast on the NMR time scale, only a single spin−lattice relaxation rate will result, corresponding to a pore size located between R_1 and R_2. The term "fast on a NMR time scale" means fast with respect to T_1 (range of ms). Assuming a diffusivity of $D \approx 10^{-5}$ cm² s⁻¹ (bulk D_2O diffusion), the molecules will diffuse a distance of approximately $r \approx 10^4$ Å during $t = 1$ ms (using the Einstein equation; $r^2 \approx 6Dt$), which is much larger than the pore dimension. Hence, the model equation, represented by eq 12d, will not enable the two dimensions R_1 and R_2 to be extracted. Only an average pore dimension R ($R_1 < R < R_2$) will result. If the porous material is characterized by a distribution of pore sizes, in which the confined fluid diffuses fast on a NMR time scale, only a single spin−lattice relaxation rate will result. Hence, only a single, average pore size will be extracted.

This suggests that a better approach to correlate spin−lattice relaxation rate and pore size is to use the average spin−lattice relaxation rate, as determined from the continuous relaxation model, and the average pore dimension, as obtained from N_2 adsorption. This is illustrated by the solid curve in Figure 8, which gives $1/T_{1s} = 39.5$ s⁻¹ and $1/T_{1b} = 2.0$ s⁻¹. The value of d ($=3.8$ Å) was taken from the cryogenic NMR analysis (see previous section) and kept fixed during curve fitting to eq 12d.

From such a calibration procedure, the PSD from relaxation time measurements may be derived under the assumption that diffusion of fluid molecules between the different pores is slow on the NMR time scale. This means that the pore connectivity is poor. This will be discussed in the next section.

3.6. PSD from Spin−Lattice Relaxation Time Measurements. Noting that the number of water molecules (dN) having relaxation rates between $1/T_1$ and $1/T_1 + d(1/T_1)$ can be written

$$dN = f(1/T_1)\,d(1/T_1) = g(1/R)\,d(1/R) = -h(R)\,dR \tag{13}$$

where $h(R)$ and $g(1/R)$ represent the PSD and the inverse PSD, respectively, we find that $h(R) = g(1/R)/R^2$. Equation 13 can be rearranged to read

$$g(1/R) = 2df(1/T_1)\,\sqrt{(1/T_{1s} - 1/T_1)(1/T_{1s} - 1/T_{1B})} \tag{14}$$

PSD derived from eq 14 is illustrated by the solid curves in Figure 9 and suggests the PSD derived from NMRT to be narrower than the corresponding PSD derived from cryogenic NMR. However, the average pore dimensions extracted from the two techniques are approximately the same. From the discussion presented in the previous section, we tentatively believe this difference to originate from poor pore connectivity; that is, water molecules diffuse between the different pores on a time scale which is slow on the NMR time scale. This
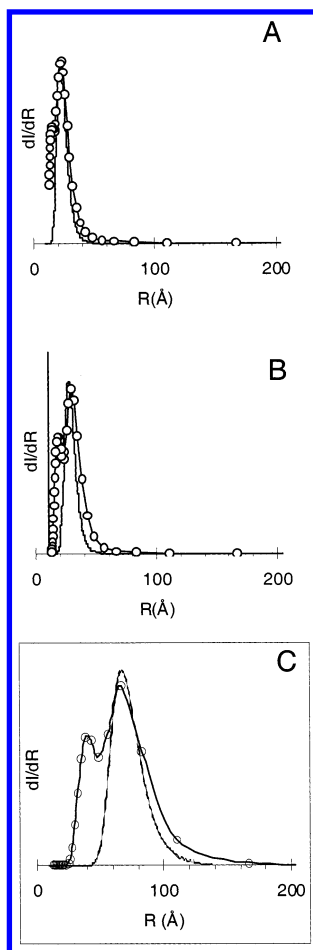
Figure 9. PSD of samples S40 (A), S60 (B), and S100 (C) as obtained by cryogenic NMR (O; solid curves) and NMRT (dotted curves).
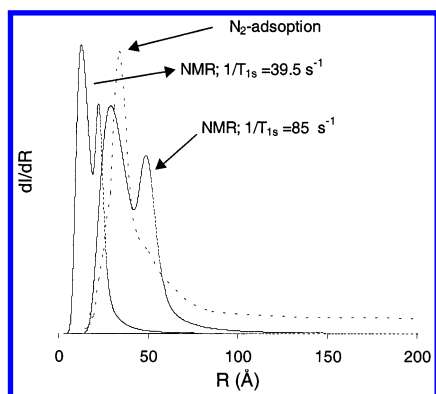

Figure 10. PSD of pure TiO_2 obtained by N_2 adsorption (- - -) and NMRT (—). Two PSD curves are derived from the NMRT approach differing only in their value of the surface spin−lattice relaxation rate $1/T_{1s}$. See text for further details.

observation suggests that NMRT (using D_2O as a probe molecule) is restricted mainly to probe average pore sizes, unless the pores are completely isolated; that is, no pore connectivity exists, or/and the diffusivity of fluid is slow on a NMR time scale.

4. PSD of a Supported TiO_2 Membrane

The PSD of a pure TiO_2 membrane, as derived from N_2 adsorption, is shown as a dotted curve in Figure 10. The corresponding PSD obtained by NMRT is shown by the solid curves for two different values of $1/T_{1s}$: $1/T_{1s} = 39.5$ s^{-1} (left) and $1/T_{1s} = 85$ s^{-1} (right). The curve with the larger relaxation
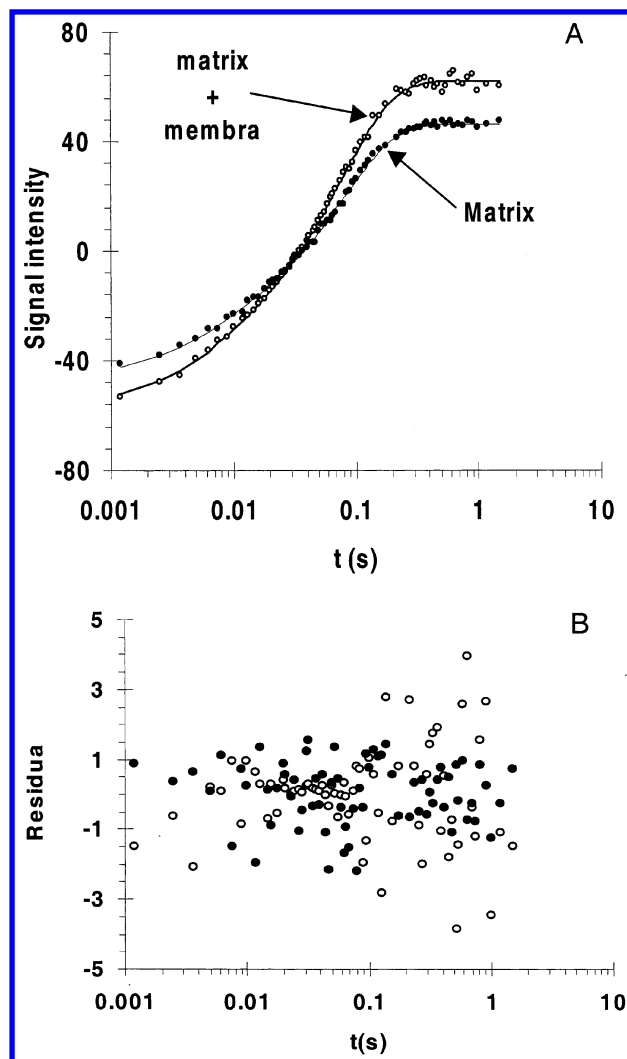

Figure 11. (A) Spin−lattice relaxation curves of a TiO_2 membrane on a silica support (O) and a "pure" silica support (●). The solid curve belonging to the latter data represents a model fit to a discrete relaxation model, I_{matrix} composed of two exponentials (eq 8 with $I = 2$). The solid curve belonging to the former data set (matrix + membrane) represents a model fit to eq 15. See text for further details. (B) Residual fits obtained by model fitting.

rate gives a significantly better fit to the PSD derived from N_2 adsorption, suggesting the relaxation strength between D_2O and TiO_2 to be different from the corresponding relaxation strength between D_2O and SiO_2. This observation must be kept in mind when analyzing the relaxation curve of materials containing both TiO_2 and SiO_2. Although this complicates the NMR analysis, it is still possible to separate the two effects under certain precautions.

For instance, the observed spin−lattice relaxation curve of a silica matrix is shown as black dots (●) in Figure 11. The solid curve was calculated by a nonlinear least-squares fit to a sum of two exponential functions (eq 8 with $i = 2$), denoted I_{matrix}.

Correspondingly, the TiO_2 membrane on a silica support (the matrix) reveals a relaxation curve shown by open dots in Figure 11A. If we denote the relaxation curve of the membrane by $I_{membrane}$, the relaxation curve of the system, membrane + matrix, can be written

$$I = \alpha I_{matrix} + \beta I_{membrane} \qquad (15)$$

The best fit to the observed data points (open dots) is shown by the solid curve with the signal intensity of the membrane

constituting approximately 15% of the total signal intensity. The derived relaxation rate ($1/T_{1,membrane}$) of the pore-confined water within the membrane was found to be 0.061 s^{-1} and corresponds to an average pore radius of approximately 42 Å. Using a model containing more than one single relaxation rate did not statistically improve the fit.

Also, the residuals shown in Figure 11B reveal a random error distribution.

This pore radius is in reasonable agreement with what is observed by N$_2$ adsorption (Figure 10). Again we notice that only an average pore dimension of the membrane is derived by the spin−lattice relaxation technique. A distribution was not possible to obtain and suggests a significant connectivity between pores to exist within the membrane material.

It must be pointed out that the pore dimension by this NMRT technique was estimated from eq 12d, under the constraint that the surface relaxation rate was equal to 85 s^{-1} (see Figure 10) and is discussed in a previous section.

To our knowledge, the approach presented in this section represents a first attempt to estimate the pore dimension of a membrane on a silica support by ^{2}H NMRT. We believe, however, that cryogenic NMR is the better choice for determination of PSD. NMRT is, however, a quick way of estimating the average pore dimension of a porous material. It has to be emphasized, however, that PSD derived from NMRT may differ from the corresponding PSD obtained by N$_2$ adsorption or cryogenic NMR because of a combined effect of pore connectivity and fluid diffusion within the pore space.

5. Conclusion

The melting point distribution and spin−lattice relaxation distribution obtained by cryogenic NMR and NMRT of porous materials saturated with D$_2$O enables the PSD to be derived, independently. Both methods require, however, a relation between the actual NMR parameters (melting point and spin−lattice relaxation rate) and the pore dimension. This correlation must be established by an independent experimental technique.

In this work, N$_2$ adsorption has been chosen as this second reference technique. It must be kept in mind that N$_2$ adsorption might not be the ultimate or best choice, because of this technique's crucial and inherent dependence on well-known pore geometry.

However, the work presented shows that cryogenic NMR and N$_2$ adsorption gives similar PSD, whereas NMRT and N$_2$ adsorption gives PSD, which are somewhat different with respect to the width of the distributions. This observation suggests that the two NMR techniques probe the pore space differently. Hence, we believe that a combined use of cryogenic NMR and NMRT may give important information both on the PSD and on the pore connectivity. Further studies are initiated to identify to what extent cryogenic NMR and NMRT may probe these parameters simultaneously. Well-characterized porous materials of the MCM-41 type will be used in such an investigation.

Appendix

Denoting the spin−lattice relaxation rates $1/T_1$ by x, eq 9 can be written

$$M(\tau) = \int_{x_B}^{x_S} M_0[1 - \alpha \exp(-\tau x)]f(x)\, dx \quad (A1)$$

assuming a Gaussian distribution function $f(x)$

$$f(x) = I_0 \frac{1}{\sqrt{2\pi}\sigma} \exp\left[-\left(\frac{x - \bar{x}}{\sqrt{2}\sigma}\right)^2\right] \quad (A2)$$

eq A1 can be rewritten as

$$M(\tau) = \frac{M_0 I_0}{\sqrt{2\pi}\sigma}\left(\int_{x_B}^{x_S} \exp\left[-\left(\frac{x - \bar{x}}{\sqrt{2}\sigma}\right)^2\right] dx + \right.$$
$$\left. \alpha \int_{x_B}^{x_S} \exp(-x\tau) \exp\left[-\left(\frac{x - \bar{x}}{\sqrt{2}\sigma}\right)^2\right]\right) dx \quad (A3)$$

The first term can be easily evaluated by introducing the error function, erf(x)

$$\text{erf}(x) = \int_0^x \exp[-z^2]\, dz \quad (A4)$$

The latter term under the integral sign can be written as

$$\exp(-x\tau) \exp\left[-\left(\frac{x - \bar{x}}{\sqrt{2}\sigma}\right)^2\right] = \exp\left[-\left\langle\frac{x - (\bar{x} - \sigma^2\tau)}{\sqrt{2}\sigma}\right\rangle^2 + \right.$$
$$\left. \left\langle\frac{1}{2}\sigma^2\tau^2 - \bar{x}\right\rangle\right] \quad (A5)$$

Introducing the following notations

$$\bar{x}' = \bar{x} - \sigma^2\tau \quad (A6a)$$

$$\beta = \sigma_i \tau^2/2 - \tau\bar{x}. \quad (A6b)$$

eq A5 can be written

$$\exp(-x\tau) \exp\left[-\left(\frac{x - \bar{x}}{\sqrt{2}\sigma}\right)^2\right] = \exp[\beta] \exp\left[-\left\langle\frac{x - \bar{x}'}{\sqrt{2}\sigma}\right\rangle^2\right] \quad (A7)$$

Inserting eq A7 into eq A3 gives eq 11, which has been calculated in Excel spreadsheet by applying the Erf function (eq A4).

References and Notes

(1) Brown, R. J. S. *Am. Phys. Soc. Bull. Ser. II* **1956**, 216.

(2) Sentura, S. D.; Robinson, J. D. *Soc. Pet. Eng. J.* **1970**, *10*, 237.

(3) Brownstein, K. R.; Tarr, C. E. *J. Magn. Res.* **1977**, *27*, 17.

(4) Almagor, E.; Belfort, G. *J. Colloid Interface Sci.* **1978**, *66*, 146.

(5) Cohen, M. H.; Mendelson, K. S. *J. Appl. Phys.* **1982**, *53*, 1127.

(6) Tarczon, J. C.; Halperin, W. P. *Phys. Rev. B* **1985**, *32*, 2798.

(7) Schmidt, E. J.; Velasco, K. K.; Nur, A. M. *J. Appl. Phys.* **1986**, *59*, 2788.

(8) Gallegos, D. P.; Munn, K., Smith, D. M.; Sterner, D. L. *J. Colloid Interface Sci.* **1987**, *119*, 127.

(9) Schmidt, R.; Stöcker, M.; Hansen, E. W.; Akporiaye, D.; Ellestad, O. H. *Microporous Mater.* **1995**, *3*, 443.

(10) Hansen, E. W.; Stöcker, M.; Schmidt, R.; Akporiaye, D. *J. Phys. Chem.* **1996**, *100*, 2195.

(11) Hansen, E. W.; Schmidt, R.; Stöcker, M. *J. Phys. Chem.* **1996**, *100*, 11396.

(12) Hansen, E. W.; Tangstad, E.; Myrvold, E.; Myrstad, T. *J. Phys. Chem. B* **1997**, *101*, 10709.

(13) Ito, T.; Fraissard, J. *J. Chem. Phys.* **1982**, *76*, 5225.

(14) Cotts, R. M.; Hoch, M. J. R.; Sun, T.; Markert, J. T. *J. Magn. Res.* **1989**, *83*, 252.

(15) Latour, L. L.; Li, L.; Sotak, C. H. *J. Magn. Res. Ser. B* **1993**, *101*, 72.

(16) Gladden, L. F. *Trans. Inst. Chem. Eng. Part A* **1993**, *71*, 657−674.

(17) D'Orazio, F.; Tarczon, J. C.; Halperin, W. P.; Eguchi, K.; Mizusaki, T. *J. Appl. Phys*. **1989**, *65(2)*, 742.

(18) Gallegos, D. P.; Smith, D. M. *J. Colloid Interface Sci*. **1988**, *122*, 143.

(19) Bhattacharja, S.; Moukawa, M.; D'Orazio, F.; Jehng, J.; Halperin, W. P. *Adv. Cement Based Mater.* **1993**, *1*, 67−76.

(20) Schreiner, L. J.; Mactavish, J. C.; Miljković, L.; Pintar, M. M.; Blinc, R.; Lahajnar, G.; Reeves, L. W. *J. Am. Ceram. Soc.* **1985**, *68*, 10.

(21) Kleinberg, R. L.; Kenyon, W. E.; Mitra, P. P. *J. Magn. Res. Ser. A* **1994**, *108*, 195.

(22) Glasel, J. A.; Lee, K. H. *J. Am. Chem. Soc.* **1974**, *96*, 979.

(23) Look, J. L.; Bogush, G. H.; Zukoski, C. F. *Faraday Discuss. Chem. Soc.* **1990**, *90*, 345.

(24) Abragam, A. *Principles of Nuclear Magnetism*; Oxford University Press: Oxford, U.K., 1961.

(25) Brunauer, S.; Emmett, P. H.; Teller, E. *J. Am. Chem. Soc.* **1938**, *50*, 309.

(26) Barrett, E. P.; Joyner, L. G.; Halenda, P. P. *J. Am. Chem. Soc.* **1951**, *73*, 373.

(27) Kruk, M.; Jaroniec, M.; Gilpin, R. K.; Zhou, Y. W. *Langmuir* **1997**, *13*, 545.

(28) Kruk, M.; Jaroniec, M.; Sayari, A. *Langmuir* **1997**, *13*, 6267.

(29) Gibbs, J. W. *Collected Works*; Longmans: Green, New York, 1928.

(30) Thompson, W. (Lord Kelvin) *Philos. Mag.* **1871**, *42*, 448.

(31) Kowalevski, J.; Larsson, T.; Wesltlund, P.-O. *J. Magn. Reson.* **1987**, 77.

(32) Watson, A. T.; Chang, C. T. P. *Prog. Nucl. Magn. Reson. Spectrosc.* **1997**, *31*, 343.

(33) Wahba, G. *J. Numer. Anal.* **1977**, *14*, 651.

(34) Zimmermann, J. R.; Brittin, W. E. *J. Phys. Chem.* **1957**, *61*, 1328.